Front. Optoelectron. 2021, 14(4): 426–437
https://doi.org/10.1007/s12200-020-1010-6

RESEARCH ARTICLE

# Optical generation of UWB pulses utilizing Fano resonance modulation

**Zhe XU, Yanyang ZHOU, Shuhuang CHEN, Liangjun LU, Gangqiang ZHOU, Jianping CHEN, Linjie ZHOU (✉)**

State Key Laboratory of Advanced Optical Communication Systems and Networks, Shanghai Key Laboratory of Navigation and Location Services, Shanghai Institute for Advanced Communication and Data Science, Department of Electronic Engineering, Shanghai Jiao Tong University, Shanghai 200240, China



**Abstract** In this paper, we reported an integrated method to generate ultra-wideband (UWB) pulses of different orders based on a reconfigurable silicon micro-ring resonator-coupled Mach–Zehnder interferometer. Under proper operating conditions, the device can produce Fano resonances with a peak-to-valley extinction ratio of above 20 dB. UWB monocycle and doublet signals with picosecond pulse widths are produced when the micro-ring resonator is modulated by square and Gaussian electrical pulses, respectively. With our Fano resonance modulator on silicon photonics, it is promising to foresee versatile on-chip microwave signal generation.

**Keywords** ultra-wideband (UWB) generation, Fano resonance, intensity modulation, integrated silicon modulator

## 1 Introduction

Microwave photonics have developed rapidly in recent years [1,2]. Many functions have been demonstrated, including ultra-wideband (UWB) signal generation [3], reconfigurable high-resolution radio frequency (RF) filtering [4], RF phase shifts [5], RF frequency up-conversion [6], and optical phased array beamforming [7]. Microwave photonic systems based on bulky optical components have suffered from a large volume, high-power consumption, high cost, and vulnerability to environmental disturbances. Therefore, it is highly desirable to integrate a microwave photonics system into a single chip to make it more compact, less expensive, and less power consuming.

Received February 4, 2020; accepted June 22, 2020

E-mail: ljzhou@sjtu.edu.cn

Wideband communication dates back to the beginning of the 20th century in which spark-gap transmitters were used in World War I. However, in the 1920s, it was quickly replaced by superheterodyne radio, which can send continuous signals. Another wireless wideband technology, radar, developed rapidly, inspiring interest in signals with an ultra-wide bandwidth.

UWB signals have inherent characteristics, such as immunity to multipath fading, a wide bandwidth, and low-power spectral density [8]. One of its applications is in short-range high-throughput wireless communication (IEEE 802.15.3a) for wireless transmission of massive multimedia data without delay. It can also be used in low-speed and low-power transmission (IEEE 802.15.4a) for Internet of Things (IoT) applications, such as precise indoor positioning. Unlike WiFi- or Bluetooth-based distance estimation depending on the intensity of the signal, the UWB signal has an extremely narrow pulse width, which is similar to a radar pulse, making it possible to predict the position with an accuracy of 10 cm using the signal propagation time [9]. The Federal Communication Commission (FCC) provided UWB signal regulation in 2002 [10], and Apple Inc. has applied UWB technology in its products, such as iPod and iWatch. Many other companies, including NXP, Samsung, Bosch, Sony, and others, have formed an organization called the FiRa consortium to promote UWB application for perfect user experiences for circumstances, such as hands-free access control, location-based services, and device-to-device (peer-to-peer) services [11].

Traditional UWB pulse generation via electrical circuits needs electrical-to-optical conversion to distribute the signal over an optical fiber. Generating UWB signals directly in the optical domain with integrated photonics has many merits, including its light weight, small size, large tunability, and immunity to electromagnetic interference

[3]. Several optical methods have been reported to produce UWB pulses, the most common of which is to implement phase-to-intensity modulation via dispersive devices [12] or frequency discriminators [13], such as a bandpass filter [14] or an fiber-Bragg-grating (FBG) [3,15]. Some others have obtained UWB pulses of different orders from the derivative of Gaussian pulses [16], and factors related to power efficiency were analyzed [17]. Furthermore, many studies have focused on coherent [13,16,18–20] and incoherent [14] summation of UWB signals of low orders to generate UWB pulses of higher orders. However, these approaches all require complicated bulky systems to generate stable signals. Linear summation of modified doublet pulses can be utilized for high-power efficiency UWB generation [21]. Other approaches to generate UWB signals have also been proposed by using nonlinear optical loop mirrors [22] or two-photon absorption in a silicon waveguide [23]. However, these approaches all require complicated bulky systems to generate stable signals. As for the integrated method, Wang and Yao proposed a simple method to generate UWB doublet signals using an electro-optic intensity modulator (EOM) [24]. Many have reported integrated schemes to generate UWB pulses that utilize cross-phase modulation in semiconductor optical amplifiers (SOAs) [25–27], which involve a complex system and costly device fabrication. The same shortcomings also exist for electroabsorption modulator (EAM)-based methods [28,29]. For simplicity, UWB signals can be generated using a single micro-ring resonator (MRR) [30,31]. However, the essential principle is to transform phase modulation to intensity modulation (PM-IM), and the integrated MRR only plays the role of IM conversion rather than complete key function. There are also some other special methods [32,33], such as splitting the light-wave and then combining them after certain processing to produce UWB signals; however, the waveform generated is limited [32]. Other schemes [12,33] need two lasers, which increase the system volume and cost. The effect of free-carrier dispersion (FCD) and free-carrier absorption (FCA) in silicon on generated UWB signals have also been studied [34]. Monocycle pulses have been produced on a silicon photonic chip [30]. These methods are either unstable or impractical owing to the bulky system or are monotonous because only limited waveforms are generated.

The obvious feature of UWB signals is its asymmetric line shape in the time domain. It is thus straightforward to use the asymmetric Fano resonance to generate UWB signals. Fano resonance is a ubiquitous physics phenomenon in nature, which was first observed by Beutler as spectral atomic lines that exhibit sharp asymmetric profiles in absorption. Later, Miroshnichenko et al. suggested the first theoretical explanation for this effect and suggested a formula that predicts the shape of spectral lines [35]. Since then, many researchers have studied it, and Fano resonances in various systems have been discovered and analyzed. As for photonic nanostructures, devices, such as dual-bus waveguide coupled MRR [36], the bent waveguide-based Fabry–Perot resonator [37], the waveguide micro-ring Fano resonator [38], the silicon Bragg reflector [39], MRR with a feedback coupled waveguide [40], add-drop MRR [41,42], a nanobeam cavity [43,44], coupled whispering-gallery-mode resonators [44,45], and the plasmonic resonator [46], have been proposed to produce Fano resonance. These have many applications in switching [43], sensing [39], photonic thermometers [38], instantaneous microwave frequency measurement [47], and others owing to the sharp asymmetric resonance line shape.

In this paper, we present a simple method to generate UWB pulses of different orders by utilizing a reconfigurable micro-ring resonator-coupled Mach–Zehnder interferometer (RC-MZI). The spectrum of the RC-MZI exhibits different line shapes when the phase difference between two arms of the MZI varies. Modulation is performed by the MRR when the device works at the Fano resonance with an asymmetric resonance line shape. UWB monocycle and doublet pulses are generated by using square and Gaussian electrical pulses, respectively. When the amplitude of the driving signal is further enlarged, UWB pulses of higher orders can also be generated.

## 2 Device structure and Fano resonance

### 2.1 Device structure

Figure 1(a) shows a schematic structure of the RC-MZI. The coupling between the MRR and the MZI (parent MZI) is enabled by a small child MZI coupler with two micro-heaters integrated for coupling tuning (indicated by the dashed box). A PN junction is integrated in the racetrack MRR for high-speed modulation. The other arm of the parent MZI is integrated with a thermo–optic phase shifter and a PIN diode-based variable optical attenuator (VOA) to adjust the phase and amplitude of the light traveling in this path, respectively. The device is highly reconfigurable, and the resonance spectrum can be flexibly tailored.

The phase shifter is enabled by a silicon resistive micro-heater that is made of a $N^{++}$-doped silicon slab, as shown in the inset of Fig. 1(a). After the current injection, the temperature of the adjacent silicon waveguide increases, leading to an increase in the effective refractive index and thus the phase of the optical beam. The phase difference between the two arms of the parent MZI determines the resonance line shape at a certain wavelength [41,48]. To obtain a high modulation efficiency, the PN junction has an L-shape cross section to maximize the overlap between the optical mode and the depletion region of the PN junction [49].

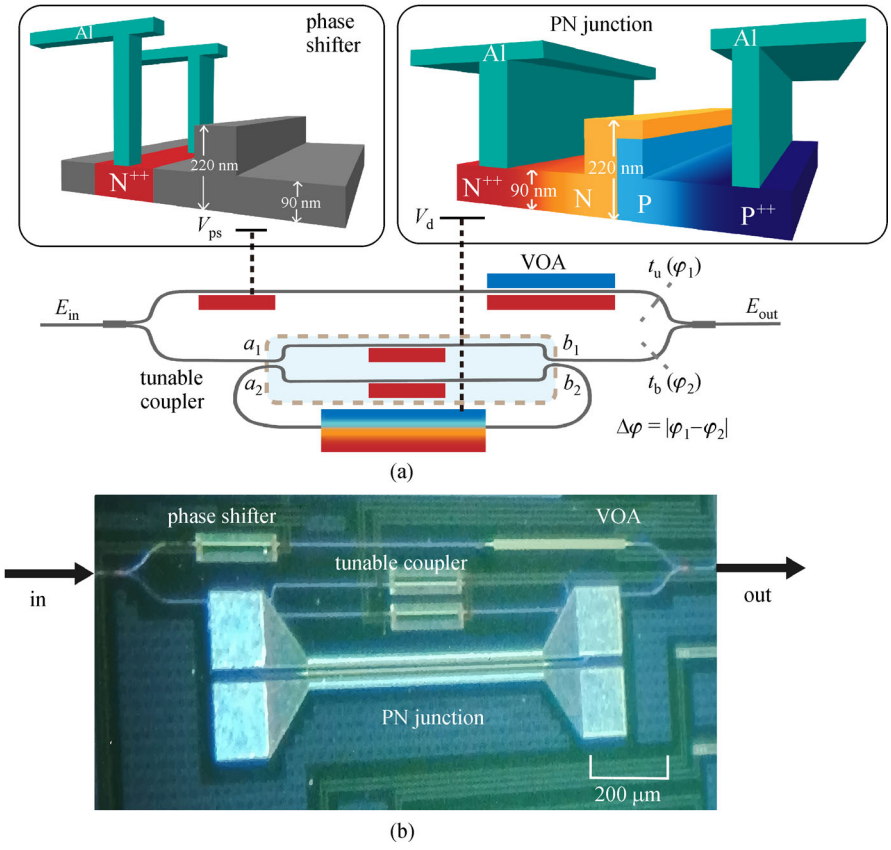


**Fig. 1** (a) Schematic structure of the micro-ring resonator-coupled Mach–Zehnder interferometer. Insets: structures of the phase shifter and the PN junction. (b) Microscope image of the fabricated device

Figure 1(b) shows a microscope image of the device. The device was fabricated using CMOS-compatible processes. Direct current (DC) and RF signals were applied to the device to set the operation point and perform the modulation, respectively. The PN junction, thermo–optic phase shifter, and VOA are 500, 200, and 300 μm in length, respectively.

## 2.2 Modeling

We used the transfer matrix method to model the device. The optical field transmission through the child MZI coupler can be described as

$$\begin{bmatrix} b_1 \\ b_2 \end{bmatrix} = \boldsymbol{M}_{\mathrm{DC}} \cdot \boldsymbol{M}_{\mathrm{MZI}} \cdot \boldsymbol{M}_{\mathrm{DC}} \cdot \begin{bmatrix} a_1 \\ a_2 \end{bmatrix}$$

$$= \begin{bmatrix} t & \mathrm{i}\kappa \\ \mathrm{i}\kappa & t \end{bmatrix} \begin{bmatrix} \mathrm{e}^{\mathrm{i}\varphi_1} & 0 \\ 0 & \mathrm{e}^{\mathrm{i}\varphi_2} \end{bmatrix} \begin{bmatrix} t & \mathrm{i}\kappa \\ \mathrm{i}\kappa & t \end{bmatrix} \cdot \begin{bmatrix} a_1 \\ a_2 \end{bmatrix}$$

$$= \begin{bmatrix} t_{11} & k_{12} \\ k_{21} & t_{22} \end{bmatrix} \cdot \begin{bmatrix} a_1 \\ a_2 \end{bmatrix}, \tag{1}$$

where $a_i$ and $b_i$ ($i$ = 1, 2) represent the light fields at the input and output ports, respectively, $\kappa$ and $t$ are the coupling and transmission coefficients of the input splitter and output combiner ($\kappa^2 + t^2 = 1$ for lossless coupling) of the child MZI, and $\varphi_i$ is the phase of the MZI arm.

Fields $a_2$ and $b_2$ are related to the racetrack ring resonator; therefore, we have

$$a_2 = b_2 \cdot a_{\mathrm{Ring}} \cdot \mathrm{e}^{\mathrm{i}\varphi_{\mathrm{Ring}}}, \tag{2}$$

where $a_{\mathrm{Ring}}$ and $\varphi_{\mathrm{Ring}}$ are the loss factor and the accumulated phase when light passes the feedback ring waveguide, respectively. From Eqs. (1) and (2), the optical field transmission through the resonance arm of the parent MZI can be written as

$$t_{\mathrm{b}} = \frac{b_1}{a_1} = t_{11} + \frac{k_{12} \cdot k_{21} \cdot a_{\mathrm{Ring}} \cdot \mathrm{e}^{\mathrm{i}\varphi_{\mathrm{Ring}}}}{1 - t_{22} \cdot a_{\mathrm{Ring}} \cdot \mathrm{e}^{\mathrm{i}\varphi_{\mathrm{Ring}}}}. \tag{3}$$

The optical field traveling through the reference arm of the parent MZI is given by

$$t_{\mathrm{u}} = a_{\mathrm{VOA}} \cdot a_{\mathrm{wg}} \cdot \mathrm{e}^{\mathrm{i}(\varphi_{\mathrm{ps}} + \varphi_{\mathrm{VOA}} + \varphi_{\mathrm{wg}})}, \tag{4}$$

where $a_{\mathrm{VOA}}$ and $a_{\mathrm{wg}}$ represent the loss factor associated with the VOA and the waveguide, respectively, and $\varphi_{\mathrm{ps}}$, $\varphi_{\mathrm{VOA}}$, and $\varphi_{\mathrm{wg}}$ are the phases of the phase shifter, the

VOA, and the waveguide, respectively. The optical field transfer function of the entire device can then be given by

$$\frac{E_{\text{out}}}{E_{\text{in}}} = \frac{1}{2}(t_{\text{u}} + t_{\text{b}}). \quad (5)$$

### 2.3 Fano resonance and modulation

Depending on the phase difference between the two arms of the parent MZI, the device can exhibit various resonance line shapes. In particular, Fano resonances are generated when the phase of the resonance path differs by π/2 or 3π/2 from the other reference path, that is, $|\varphi_1 - \varphi_2| = \pi/2$ or 3π/2, where $\varphi_1$ and $\varphi_2$ are the arm phases of the parent MZI. At the Fano resonances, the output spectrum presents asymmetric resonance line shapes [41,48].

After applying an RF driving signal on the PN junction, UWB pulses can be generated by modulating at the Fano resonances. As depicted in Figs. 2(a) and 2(b), the Fano resonance spectrum shifts back and forth in response to the electrical driving signal. Effectively, the operation point moves along the Fano spectrum on the rising/falling edge of the square-wave driving signal. Thus, following the Fano resonance line shape, the output optical power varies correspondingly to produce a pair of monocycle UWB pulses of opposite polarities in the time domain.

When the RF driving signal is a Gaussian pulse, the device generates a UWB doublet signal, as shown in Fig. 2(c). The symmetric-looking UWB doublet pulses are produced when the halves of the two monocycle UWB pulses in opposite polarities are combined. The upside-down inverted UWB doublet can also be generated by modulating the Fano resonance with a difference in the π-phase (see Fig. 2(d)).

## 3 Measurement and results

### 3.1 Transmission spectrum

We first measured the device transmission spectrum, as shown in Fig. 3. Because of the arm length difference of the parent MZI, the resonance line shape varies with wavelength to cover one Fano resonance evolution cycle from 1551 to 1563 nm. The free spectral range of the MRR is approximately 0.4 nm, whereas that of the parent MZI is 11 nm. Then, owing to the interference between the MRR

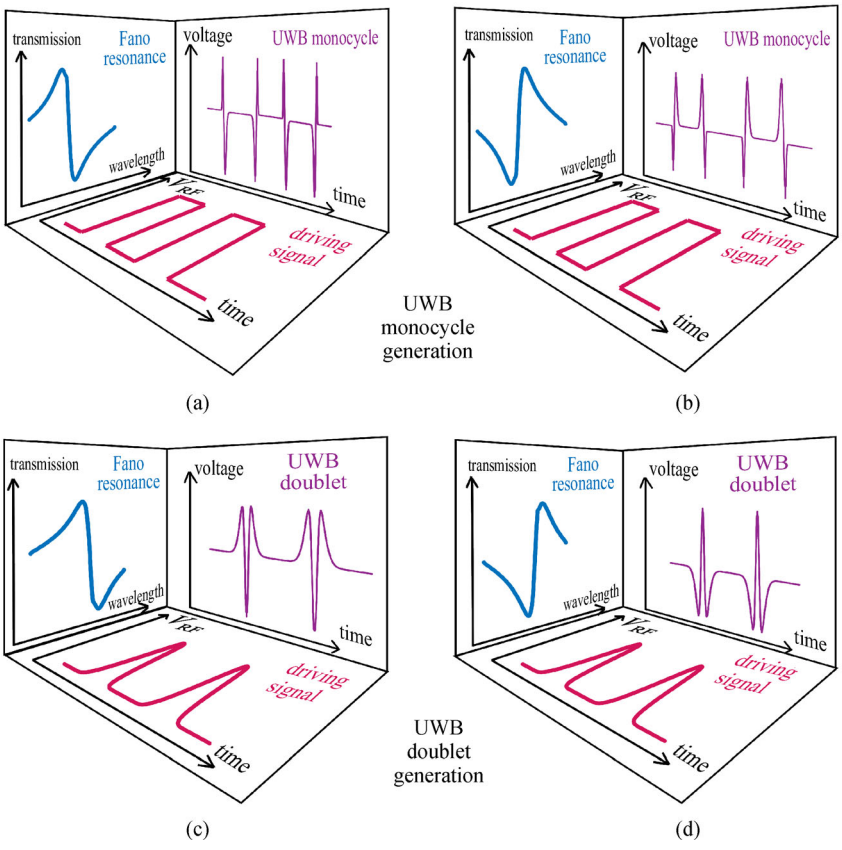


**Fig. 2** Working principle illustration for generation of (a) and (b) UWB monocycle pulses in two polarities, (c) and (d) UWB doublet pulses in two polarities

and the parent MZI, the device exhibits distinct resonance line shapes when the phase difference ($\Delta\varphi$) between the MRR and the MZI changes. Specifically, when $\Delta\varphi \approx \pi/2$, the typical asymmetric Fano resonance line shape is observed as shown in the upper left graph of Fig. 3. The asymmetric Fano resonance has a peak-to-valley extinction ratio of above 20 dB. When $\Delta\varphi \approx 3\pi/2$, it exhibits the reversed asymmetric Fano line shape, as shown in the upper right graph of Fig. 3. When $\Delta\varphi \approx \pi$, the spectrum shows an inverted Lorentzian line shape in the bottom left graph of Fig. 3. When $\Delta\varphi \approx 0$, it becomes a Lorentzian line shape as shown in the bottom right graph of Fig. 3. More detailed explanations about the Fano resonance can be found in Ref. [48].

By applying a DC voltage, $V_{ps}$, on the phase shifter, the phase difference between the arms of the parent MZI changes, generating different resonance line shapes in the spectrum, as shown in Fig. 4. Because the MRR is sensitive to temperature, the device was placed on a thermoelectric cooler during measurement to maintain the temperature at 22°C±0.05°C.

Figure 5(a) shows that the Fano resonance spectrum shifted when a DC voltage was applied onto the PN junction. When the PN junction was set under the forward bias regime ($V_d > 0$), it provided a higher modulation efficiency but a larger loss than that under the reverse bias. We extracted the phase shift from Fig. 5(a), taking the 0 V curve as the reference. Then, we calculated the variation in

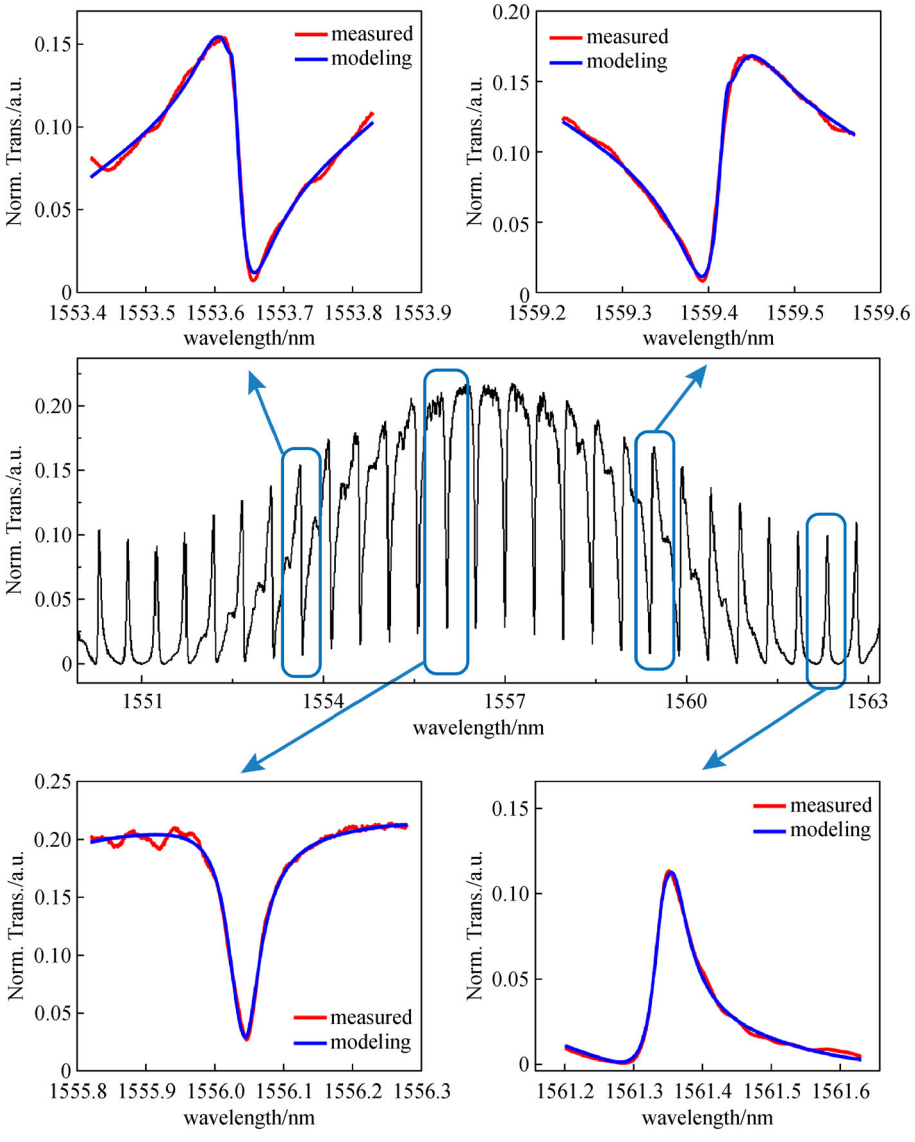


**Fig. 3** Measured transmission spectrum of the RC-MZI in one Fano resonance evolution cycle. The insets illustrate the magnified resonance spectra at different wavelengths. The modeled spectra are also shown

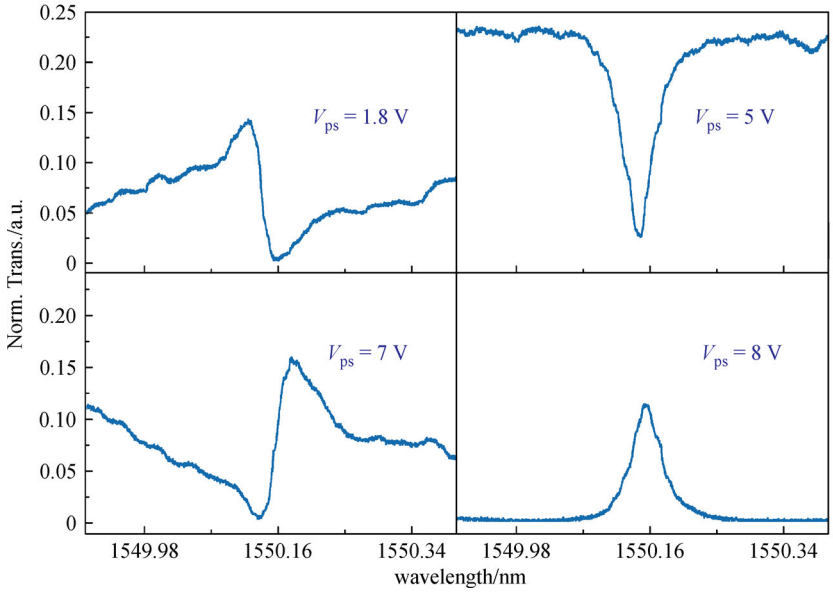


**Fig. 4** Resonance spectra at four voltages ($V_{ps}$) on the phase shifter

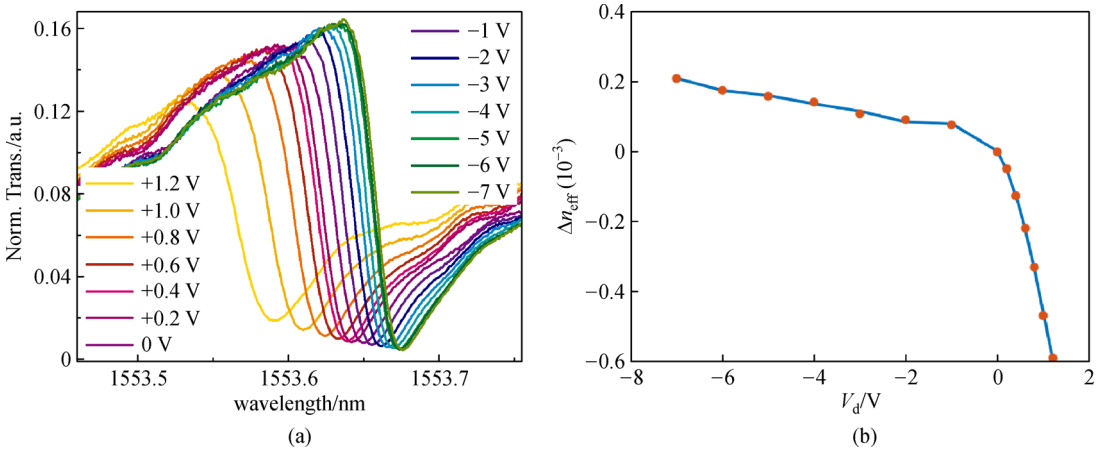


**Fig. 5** (a) Fano resonance spectral shifts with different voltages ($V_d$) applied to the PN junction. (b) Extracted waveguide effective refractive index variation as a function of voltage on the PN junction

the effective refractive index using the formula: $\Delta n_{eff} = (\lambda/2\pi)\cdot\Delta\varphi$. Figure 5(b) shows the effective refractive index change as a function of voltage. It has a slope of $-2\times10^{-5}$ and $-2.2\times10^{-4}$ $V^{-1}$ in the reverse and positive bias regimes, respectively.

### 3.2 UWB pulse generation

According to the working principle described above, we set up an experimental system to generate UWB pulses, as shown in Fig. 6. Light from a tunable continuous-wave laser (EXFO, T100S-HP, Canada) passes through a polarization controller (PC) before being coupled to the device. Square-wave or Gaussian RF pulses are generated by an arbitrary waveform generator (AWG, SHF, 19120 B, Germany), amplified by an RF amplifier (SHF 810, broadband amplifier, Germany) and then combined with the DC bias voltage through a bias-tee before they are applied to the travelling-wave electrode (TWE) of the device via a 40-GHz microwave probe for electro-optic modulation. The other end of the TWE is terminated by a 50-Ω resistor for impedance matching. The modulated optical signal output from the device is then amplified by an erbium-doped fiber amplifier (EDFA) to compensate for device insertion loss, followed by a 3-nm bandwidth optical filter to suppress the amplified spontaneous emission noise. Finally, the optical signal is received by a photodetector and measured using an oscilloscope (Keysight, Infinium UXR0804A, USA) and an electrical spectrum analyzer (ESA, R&S, FSUP 50, Germany).

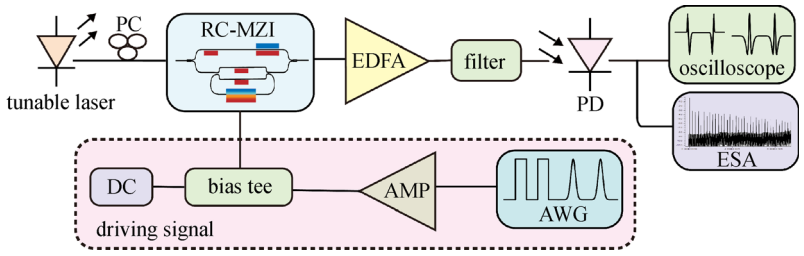


**Fig. 6** Experimental setup for UWB signal generation and characterization. PC: polarization controller, EDFA: erbium-doped fiber amplifier, PD: photodetector, AMP: RF amplifier, AWG: arbitrary waveform generator, ESA: electrical spectrum analyzer

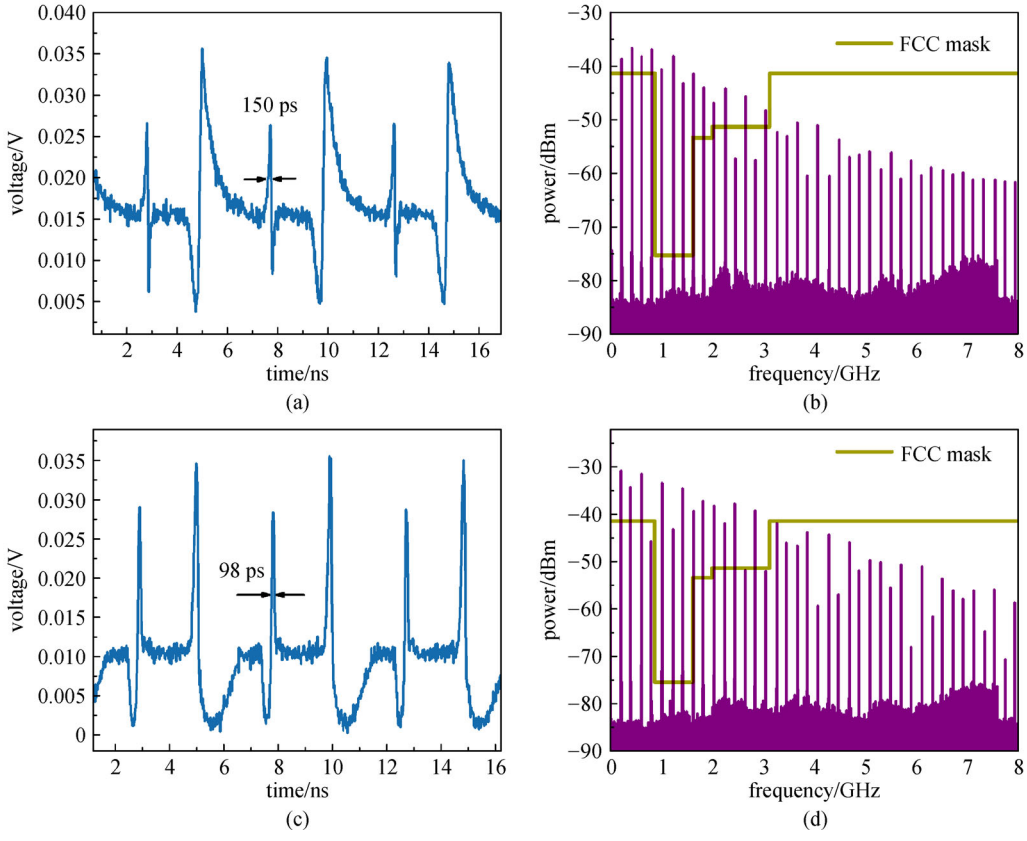


**Fig. 7** Generation of UWB monocycle pulses. (a) Monocycle pulses at the Fano resonance wavelength of 1548.93 nm and (b) its electrical spectrum. (c) Monocycle pulses at the Fano resonance wavelength of 1553.74 nm and (d) its electrical spectrum

Figure 7(a) shows the UWB monocycles generated at the wavelength of 1548.93 nm. The RF square-wave driving signal has a frequency of 200 MHz and a duty cycle of 35%. The voltage swing is from −0.94 to 2.76 V. The PN junction works mainly in the forward bias regime to utilize its high modulation efficiency. The UWB monocycle signal has a pulse width of approximately 150 ps at the rising edge of the RF signal. Because the falling edge of the driving signal is slower than the rising edge owing to the waveform distortion from the AWG, it generates a broader UWB monocycle pulse in the opposite polarity. Figure 7(c) shows the resulting UWB monocycle pulses when the device was modulated at the wavelength of 1553.74 nm. The pulse width was approximately 98 ps. Figures 7(b) and 7(d) show the RF spectra of the UWB waveforms. The discrete frequency lines have a spacing of 200 MHz, which is equal to the repetition rate of the monocycle pulses.

When the RF driving signal is altered to Gaussian pulses, UWB doublet pulses can be generated. The Gaussian pulses have a frequency of 200 MHz and a duty cycle of 15% with a voltage swing from −1 to 3.7 V. Figure 8 shows the UWB doublet signals and the corresponding RF spectra.

If we still use a square wave as the electrical driving signal and increase its voltage swing, higher-order UWB

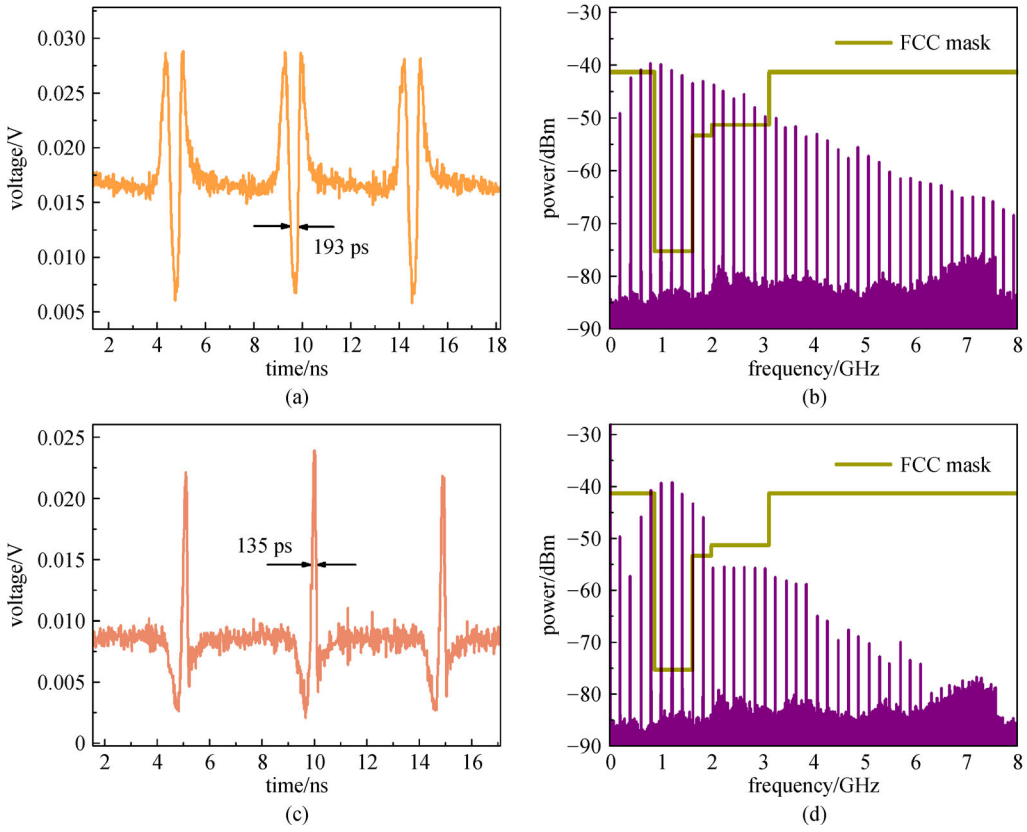


**Fig. 8** Generation of UWB doublet pulses. (a) Doublet pulses at the Fano resonance wavelength of 1548.93 nm and (b) its electrical spectrum. (c) Doublet pulses at the Fano resonance wavelength of 1553.74 nm with the opposite polarity and (d) its electrical spectrum

pulses can be generated, as shown in Fig. 9. When the driving signal voltage swing is from −1.1 to 3.9 V, the device generates UWB doublet pulses (Fig. 9(a)). When the voltage swing is from −0.7 to 4.3 V, it generates UWB triplet pulses (Fig. 9(c)). When the driving voltage is further enlarged with a swing from −1.16 to 5.16 V, UWB quadruplet pulses are generated (Fig. 9(e)). The frequency spacing in the electrical spectrum is 100 MHz, which corresponds to the repetition rate of the RF driving signal. Higher-order UWB pulses have better potential for communication applications because the interference between UWB signals and other wireless signals decreases [18].

Table 1 illustrates the extracted RF central frequencies, 10-dB bandwidths, and fractional bandwidths of the generated UWB signals. The 10-dB bandwidths of the generated UWB signals are all wider than 500 MHz, and the fractional bandwidths are over 20%, which qualifies as the basic definition of a UWB signal. The RF central frequencies are approximately 1 GHz, which is out of the bandwidth of a typical power-efficient UWB signal (from 3.1 to 10.6 GHz). Perhaps the low central frequencies of the generated UWB signals are caused by the limited electro–optic (EO) bandwidth of the modulator. Particularly, as the doublet generated by Gaussian pulses is essentially a combination of two monocycles, it is possible to produce FCC-compliant UWB pulses by tuning the full width at half maximum (FWHM) of the Gaussian pulses for the UWB doublet pulses [21,50]. Of note, there is infringement in the global positioning system band (from 0.96 to 1.61 GHz). These unwanted RF frequencies could be filtered by an UWB antenna.

## 4 Conclusions

We have realized a reconfigurable RC-MZI device on a silicon photonics platform. It can generate Fano resonances with asymmetric line shapes when there is a proper phase difference between the two arms of the parent MZI. The Fano resonance is modulated when a RF signal drives the PN junction in the MRR, producing optical UWB monocycle and doublet signals. UWB signals in opposite polarity can be easily obtained by modulating at the other asymmetric Fano resonance. Even higher-order UWB pulses can be produced when the driving signal is enhanced with a larger voltage swing. UWB technology has superior performances in terms of accuracy, power consumption, robustness in wireless connectivity, and security. It is a promising technology in the era of 5G IoT,

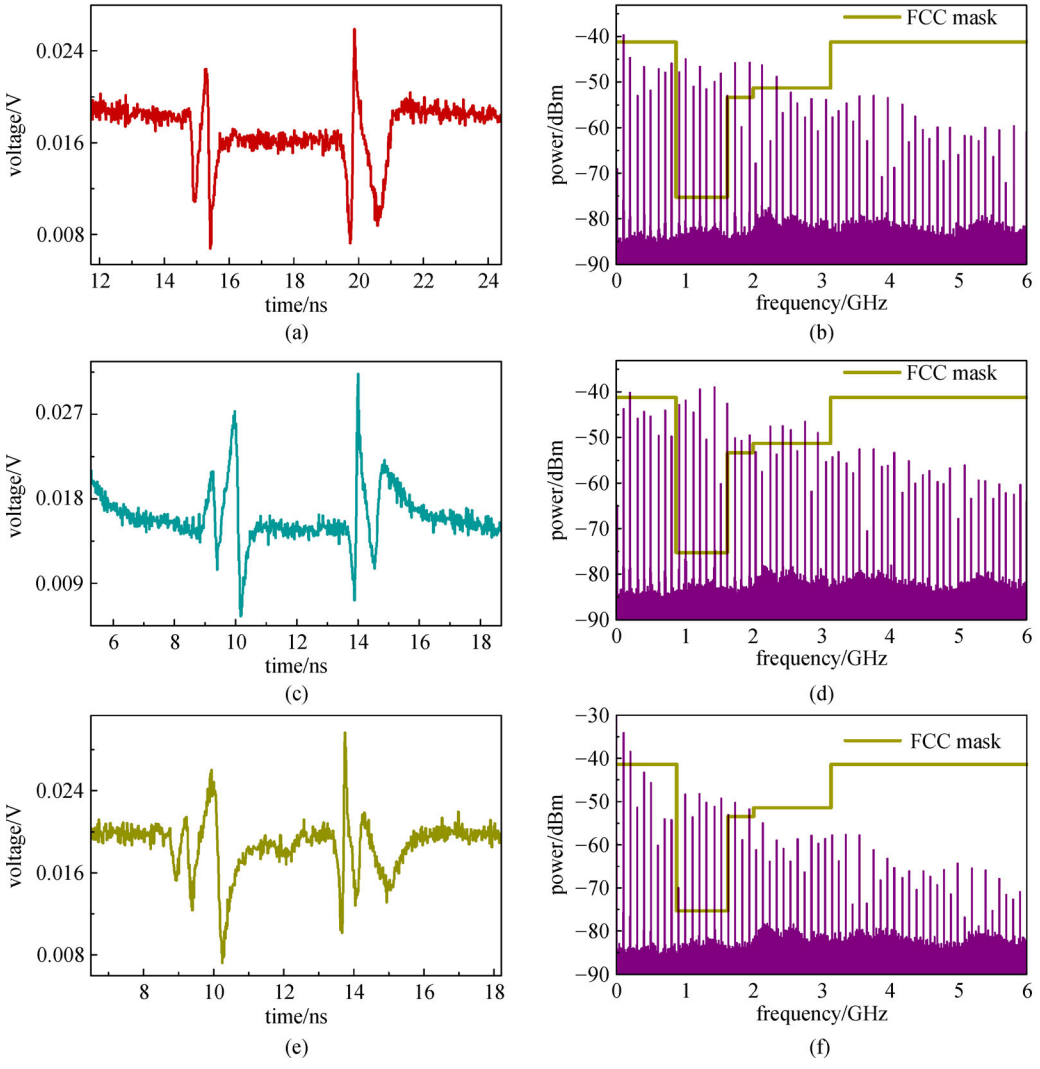


**Fig. 9** Generation of high-order UWB pulses using a square-wave driving signal. (a) and (b) UWB doublet pulses and the electrical spectrum. (c) and (d) UWB triplet pulses and the electrical spectrum. (e) and (f) UWB quadruplet pulses and the electrical spectrum

**Table 1** Extracted key performance specifications of the generated UWB pulses

| electrical driving signal | 200-MHz square wave | | 200-MHz Gaussian wave | | 100-MHz square wave | | |
|---|---|---|---|---|---|---|---|
| UWB signal | UWB monocycle | UWB monocycle | UWB doublet | UWB doublet | UWB doublet | UWB triplet | UWB quadruplet |
| optical wavelength/nm | 1548.93 | 1553.74 | 1548.93 | 1553.74 | 1548.93 | 1548.93 | 1548.93 |
| central frequency/GHz | 1.2 | 0.8 | 0.8 | 1.2 | 1 | 1.1 | 1.3 |
| 10-dB bandwidth/GHz | 2.2 | 1.4 | 3 | 1.4 | 1.2 | 0.8 | 1 |
| fractional bandwidth/% | 183 | 175 | 375 | 117 | 120 | 72.7 | 76.9 |

whose applications include industrial automation, sensing network, home/office automation, and accurate indoor positioning.

**Acknowledgements** This work was supported in part by the National Key Research and Development Program (Nos. 2019YFB2203203 and 2018YFB2201702), the National Natural Science Foundation of China (NSFC) (Grant Nos. 61705129 and 61535006), the Shanghai Municipal Science and Technology Major Project (No. 2017SHZDZX03), and the Open Project Program of Wuhan National Laboratory for Optoelectronics (No. 2019WNLOKF004).

## References

1. Marpaung D, Yao J, Capmany J. Integrated microwave photonics. Nature Photonics, 2019, 13(2): 80–90
2. Zhang W, Yao J. Silicon-based integrated microwave photonics. IEEE Journal of Quantum Electronics, 2016, 52(1): 1–12
3. Yao J, Zeng F, Wang Q. Photonic generation of ultrawideband signals. Journal of Lightwave Technology, 2007, 25(11): 3219–3235
4. Zhou L, Sun Q, Lu L, Chen J. Programmable universal microwave-photonic filter based on cascaded dual-ring assisted MZIs. In: Proceedings of Smart Photonic and Optoelectronic Integrated Circuits XX. San Francisco: SPIE, 2018, 105361G
5. Yang R, Zhou L, Wang M, Zhu H, Chen J. Application of SOI microring coupling modulation in microwave photonic phase shifters. Frontiers of Optoelectronics, 2016, 9(3): 483–488
6. Zhong Y, Zhou L, Zhou Y, Xia Y, Liu S, Lu L, Chen J, Wang X. Microwave frequency upconversion employing a coupling-modulated ring resonator. Photonics Research, 2017, 5(6): 689–694
7. Zhuang L, Roeloffzen C G H, Meijerink A, Burla M, Etten W C V. Novel ring resonator-based integrated photonic beamformer for broadband phased array receive antennas—part II: experimental prototype. Journal of Lightwave Technology, 2010, 28(1): 19–31
8. Yao J. Photonics for ultrawideband communications. IEEE Microwave Magazine, 2009, 10(4): 82–95
9. Li F. Indoor positioning and navigation chips, key technologies for next-generation smart devices. 2019. Available at mp.weixin.qq.com/s/VswdBtAifrpx69t7xG-ppw (in Chinese)
10. Federal Communication Commission. Revision of Part 15 of the Commission's Rules Regarding Ultra-Wideband Transmission Systems, 2002
11. FiRa. What UWB does. Available at firaconsortium.org/discover/what-uwb-does
12. Li J, Fu S, Xu K, Wu J, Lin J, Tang M, Shum P. Photonic ultrawideband monocycle pulse generation using a single electro-optic modulator. Optics Letters, 2008, 33(3): 288–290
13. Zhou E, Xu X, Lui K, Wong K K. A power-efficient ultra-wideband pulse generator based on multiple PM-IM conversions. IEEE Photonics Technology Letters, 2010, 22(14): 1063–1065
14. Li P, Chen H, Chen M, Xie S. Gigabit/s photonic generation, modulation, and transmission for a reconfigurable impulse radio UWB over fiber system. IEEE Photonics Journal, 2012, 4(3): 805–816
15. Zeng F, Yao J. Ultrawideband impulse radio signal generation using a high-speed electrooptic phase modulator and a fiber-Bragg-grating-based frequency discriminator. IEEE Photonics Technology Letters, 2006, 18(19): 2062–2064
16. Wang Q, Yao J. Switchable optical UWB monocycle and doublet generation using a reconfigurable photonic microwave delay-line filter. Optics Express, 2007, 15(22): 14667–14672
17. Shehata M, Mostafa H, Ismail Y. On the theoretical limits of the power efficiency of photonically generated IR-UWB waveforms. Journal of Lightwave Technology, 2018, 36(10): 2017–2023
18. Feng H, Fok M P, Xiao S, Ge J, Zhou Q, Locke M, Toole R, Hu W. A reconfigurable high-order UWB signal generation scheme using RSOA-MZI structure. IEEE Photonics Journal, 2014, 6(2): 1–7
19. Hongqian M, Muguang W, Shuisheng J. Photonic generation of power-efficient UWB pulses adaptable to multiple modulation formats using a dual-drive Mach-Zehnder modulator. In: Proceedings of the 15th International Conference on Optical Communications and Networks (ICOCN). Hangzhou: IEEE, 2016, 1–3
20. Liow T Y, Song J, Tu X, Lim A E J, Fang Q, Duan N, Yu M, Lo G Q. Silicon optical interconnect device technologies for 40 Gb/s and beyond. IEEE Journal of Selected Topics in Quantum Electronics, 2013, 19(2): 8200312
21. Abraha S T, Okonkwo C M, Tangdiongga E, Koonen A M. Power-efficient impulse radio ultrawideband pulse generator based on the linear sum of modified doublet pulses. Optics Letters, 2011, 36(12): 2363–2365
22. Luo B, Dong J, Yu Y, Zhang X. Bandwidth-tunable single-carrier UWB monocycle generation using a nonlinear optical loop mirror. IEEE Photonics Technology Letters, 2012, 24(18): 1646–1649
23. Yue Y, Huang H, Zhang L, Wang J, Yang J Y, Yilmaz O F, Levy J S, Lipson M, Willner A E. UWB monocycle pulse generation using two-photon absorption in a silicon waveguide. Optics Letters, 2012, 37(4): 551–553
24. Wang Q, Yao J. UWB doublet generation using nonlinearly-biased electro-optic intensity modulator. Electronics Letters, 2006, 42(22): 1304
25. Moreno V, Rius M, Mora J, Muriel M A, Capmany J. UWB monocycle generator based on the non-linear effects of an SOA-integrated structure. IEEE Photonics Technology Letters, 2014, 26 (7): 690–693
26. Moreno V, Connelly M J, Romero-Vivas J, Krzczanowicz L, Mora J, Muriel M A, Capmany J. Integrated 16-ps pulse generator based on a reflective SOA-EAM for UWB schemes. IEEE Photonics Technology Letters, 2016, 28(20): 2180–2182
27. Moreno V, Rius M, Mora J, Muriel M A, Capmany J. Integrable high order UWB pulse photonic generator based on cross phase modulation in a SOA-MZI. Optics Express, 2013, 21(19): 22911–22917
28. Wu T, Wu J, Choi Y, Chiu Y. Novel scheme of optical Ultra-Wide-Band generation using a single electroabsorption modulator. In: Proceedings of IEEE LEOS Annual Meeting Conference. Belek-Antalya: IEEE, 2009, 509–510
29. Kuo Y, Wu J, Chen R, Chiu Y. Photonic Ultra-wide-band doublet pulse using tapered-directional coupler integrated electroabsorption modulator. In: Proceedings of the 21st Annual Wireless and Optical Communications Conference (WOCC). Kaohsiung: IEEE, 2012, 196–197

30. Xu K, Wu X, Sung J, Cheng Z. Amplitude and phase modulation of UWB monocycle pulses on a silicon photonic chip. IEEE Photonics Technology Letters, 2016, 28(3): 248–251
31. Liu F, Wang T, Zhang Z, Qiu M, Su Y. On-chip photonic generation of ultra-wideband monocycle pulses. Electronics Letters, 2009, 45 (24): 1247–1249
32. Mirshafiei M, LaRochelle S, Rusch L A. Optical UWB waveform generation using a micro-ring resonator. IEEE Photonics Technology Letters, 2012, 24(15): 1316–1318
33. Wu X, Xu K, Zhou W, Chow C W, Tsang H K. Scalable ultra-wideband pulse generation based on silicon photonic integrated circuits. IEEE Photonics Technology Letters, 2017, 29(21): 1896–1899
34. Shao H, Chen W, Zhao Y, Chi H, Yang J, Jiang X. Performance evaluation of photonic UWB generation based on silicon MZM. Optics Express, 2012, 20(7): 7398–7403
35. Miroshnichenko A E, Flach S, Kivshar Y S. Fano resonance in nanoscale structures. Reviews of Modern Physics, 2010, 82(3): 2257–2298
36. Wang F, Wang X, Zhou H, Zhou Q, Hao Y, Jiang X, Wang M, Yang J. Fano-resonance-based Mach-Zehnder optical switch employing dual-bus coupled ring resonator as two-beam interferometer. Optics Express, 2009, 17(9): 7708–7716
37. Dyshlyuk A V. Tunable Fano-like resonances in a bent single-mode waveguide-based Fabry-Perot resonator. Optics Letters, 2019, 44 (2): 231–234
38. Zhang C, Kang G, Xiong Y, Xu T, Gu L, Gan X, Pan Y, Qu J. Photonic thermometer with a sub-millikelvin resolution and broad temperature range by waveguide-microring Fano resonance. Optics Express, 2020, 28(9): 12599–12608
39. Chang C M, Solgaard O. Fano resonances in integrated silicon Bragg reflectors for sensing applications. Optics Express, 2013, 21 (22): 27209–27218
40. Zhao G, Zhao T, Xiao H, Liu Z, Liu G, Yang J, Ren Z, Bai J, Tian Y. Tunable Fano resonances based on microring resonator with feedback coupled waveguide. Optics Express, 2016, 24(18): 20187–20195
41. Zhou L, Poon A W. Fano resonance-based electrically reconfigurable add-drop filters in silicon microring resonator-coupled Mach-Zehnder interferometers. Optics Letters, 2007, 32(7): 781–783
42. Zheng S, Ruan Z, Gao S, Long Y, Li S, He M, Zhou N, Du J, Shen L, Cai X, Wang J. Compact tunable electromagnetically induced transparency and Fano resonance on silicon platform. Optics Express, 2017, 25(21): 25655–25662
43. Cheng Z, Dong J, Zhang X. Ultra-compact optical switch using single semi-symmetric Fano nanobeam cavity. Optics Letters, 2020, 45(8): 2363
44. Dong G, Wang Y, Zhang X. High-contrast and low-power all-optical switch using Fano resonance based on a silicon nanobeam cavity. Optics Letters, 2018, 43(24): 5977
45. Zhang W, Yao J. Thermally tunable ultracompact Fano resonator on a silicon photonic chip. Optics Letters, 2018, 43(21): 5415–5418
46. Li S, Zhang Y, Song X, Wang Y, Yu L. Tunable triple Fano resonances based on multimode interference in coupled plasmonic resonator system. Optics Express, 2016, 24(14): 15351–15361
47. Zhu B, Zhang W, Pan S, Yao J. High-sensitivity instantaneous microwave frequency measurement based on a silicon photonic integrated fano resonator. Journal of Lightwave Technology, 2019, 37(11): 2527–2533
48. Limonov M F, Rybin M V, Poddubny A N, Kivshar Y S. Fano resonances in photonics. Nature Photonics, 2017, 11: 543–554
49. Zhou G, Zhou L, Zhou Y, Zhong Y, Liu S, Guo Y, Liu L, Chen J. Silicon Mach-Zehnder modulator using a highly-efficient L-shape PN junction. In: Proceedings of the 10th International Conference on Information Optics and Photonics (CIOP). Beijing: SPIE, 2018, 55
50. Li P, Chen H, Wang X, Yu H, Chen M, Xie S. Photonic generation and transmission of 2-Gbit/s power-efficient IR-UWB signals employing an electro-optic phase modulator. IEEE Photonics Technology Letters, 2013, 25(2): 144–146

**Zhe Xu** received the B.S. degree from Nanjing University of Post and Telecommunication, China in 2017 and received the master degree from Shanghai Jiao Tong University, China in 2020. Her research interests include silicon electro-optic modulators and integrated microwave photonics.

**Yanyang Zhou** received the B.S. degree in Electrical Engineering from Information Engineering University, China in 2011. He received the Ph.D. degree from Department of Electronic Engineering, Shanghai Jiao Tong University, China in 2017. His research interests include design of silicon modulators and optical communication systems.

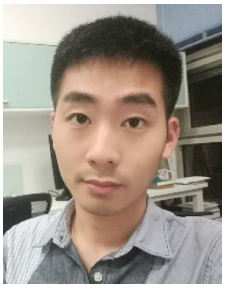

**Shuhuang Chen** received the B.S. degree from Hubei University, China in 2017 and received the master degree from Shanghai Jiao Tong University, China in 2020. His research interests include silicon electro-optic modulators and integrated microwave photonics.

**Gangqiang Zhou** received the B.S. degree from School of Physics and Optoelectronic Engineering, Xidian University, China in 2016. He is currently working toward the Ph.D. degree with State Key Laboratory of Advanced Optical Communication Systems and Networks, Department of Electronic Engineering, Shanghai Jiao Tong University, China. His research interests include silicon modulators and optical interconnection.

**Liangjun Lu** received the B.S. degree in Optical Engineering from Zhejiang University, China in 2011. He received the Ph.D. degree in Electronic Engineering from Shanghai Jiao Tong University, China in 2016. He is currently a Tenure-Track Associate Professor at State Key Laboratory of Advanced Optical Communication Systems and Networks, Shanghai Jiao Tong University, China. His research interests include silicon photonics and photonic integrated circuits.

**Jianping Chen** received the B.S. degree from Zhejiang University, China in 1983, and the M.S. and Ph.D. degrees from Shanghai Jiao Tong University, China in 1986 and 1992, respectively. He is currently a Distinguished Professor with State Key Laboratory of Advanced Optical Communication Systems and Networks, Department of Electronic Engineering, Shanghai Jiao Tong University, China. His main research interests include integrated photonic devices, photonic signal processing and precision fiber-optic time and frequency transfer. He is a Principal Scientist of the 973 Program in China.

**Linjie Zhou** received the B.S. degree in Microelectronics from Peking University, China in 2003. He received the Ph.D. degree in Electronic and Computer Engineering from The Hong Kong University of Science and Technology, China in 2007. From 2007 to 2009, he worked as a Postdoctoral Researcher at University of California, Davis, USA. Currently, he is a Professor with State Key Laboratory of Advanced Optical Communication Systems and Networks, Shanghai Jiao Tong University, China. His research interests include silicon photonics, plasmonic devices, and optical integration.